Micro-tensile behavior of struts extracted from an aluminum foam

Yasin Amani, Sylvain Dancette, Jutta Luksch, Anne Jung, Eric Maire

Micro-tensile behavior of struts extracted from an aluminum foam

Yasin Amani[a], Sylvain Dancette[a,]*, Jutta Luksch[b], Anne Jung[b], Eric Maire[a]

[a]*Univ Lyon, INSA Lyon, CNRS UMR5510, Laboratoire MATEIS, F-69621, Villeurbanne Cedex, France*
[b]*Saarland University, Applied Mechanics, Campus A4.2, 66123 Saarbrücken, Germany*

*Corresponding author. Tel.: +33 (0) 47 243 8541
Email address: sylvain.dancette@insa-lyon.fr (Sylvain Dancette)

Abstract
The tensile behavior of individual struts extracted from an open-cell aluminum foam is investigated here. X-ray microtomography is used to characterize the initial state of the struts in 3D, before micro-tensile testing performed under digital image correlation. A microstructure-sensitive finite element (FE) model is run afterwards, using a FE mesh conforming to the tomography volume and a constitutive model based on Gurson-Tvergaard-Needleman (GTN) porous plasticity. The model is made dependent on the local measure of intermetallic particles volume fraction in order to account for their embrittlement effect. Model and experiments delineate the first order effect of structure and shape on the plastic flow and fracture of the struts. The distribution of intermetallic particles influences fracture location only where minor variations of cross-section can be found. The model performs well at predicting the fracture zones but misses additional ingredients to assess the dispersion of yield strength among the struts.

Keywords: Aluminum foams, Intermetallics, Tomography, Damage, Finite Element Analysis

1. Introduction

Lightweight stochastic porous materials play an important role in structural, thermal and acoustic engineering fields. They hold properties such as low effective thermal conductivity [1, 2], high strength-to-weight ratio [3] and low cost of production. They may be used as efficient sound absorbers [4] but also in the packaging and crash-worthiness industries or for the production of the core of lightweight sandwich panels [5].

Most of the open-cell metal foams are produced using the investment casting procedure [6]. The constitutive properties of the solid phase of the foam can differ significantly from the properties of the corresponding bulk alloy, due for example to a lower cooling rate and higher surface to volume ratio [7, 8, 9]. Therefore, characterizing the solid phase of the foam is an important step in the global understanding of the foam behavior. Several methods have been used in this context, including nanoindentation [10, 11, 12], micro-mechanical tests on single struts

[13, 14, 15] and X-ray tomography scanning [16, 17, 18, 19] as regards non destructive imaging of the material structure. Standard nanoindentation experiments may allow to quantify the heterogeneity of local Young's modulus and hardness of the different internal phases of the struts, provided that the microstructure length scale is about ten times bigger than the intended indentation depth. The yield strength and strain hardening of the strut material can be measured by performing micro-tensile tests on single struts extracted from the foam. However, the irregular geometry of the struts often requires complex procedures to define a proper measure of stress and strain in the test [14]. X-ray tomography constitutes an efficient means to obtain the global 3D architecture of a whole foam but also to detect the presence of second phase particles or defects [12]. These data can subsequently be used to run a finite element (FE) simulation to predict the fracture properties of a foam block [20, 21, 22, 23].

While the global deformation and fracture behavior of metallic foams is rather well documented today, the role of local internal microstructure still requires some clarifications. As a matter of fact, the effect of internal defects or particles is averaged over a large volume in usual bulk engineering materials. This is not the case in architectured material such as metallic foams where the intermediate thickness of cell walls or struts is likely to highlight the heterogeneity of the local microstructure [24]. In the case of aluminum open-cell foams, the heterogeneity arises for example from the limited number of grains in individual struts [25] and from the potential presence of brittle intermetallic particles in various amounts [12, 23]. While the non destructive 3D crystallographic characterization of the grains in the struts would require a dedicated setup (e.g. Diffraction Contrast Tomography [26], out of the scope of the present paper), it has been shown that standard laboratory microtomography allows to detect the intermetallic particles when performed at the proper resolution [12].

The present paper aims at investigating the mechanical behavior of individual struts extracted from an aluminum foam. The adopted procedure consists in scanning the detailed 3D shape and microstructure of the struts using lab scale tomography at rather high resolution first, then performing the micro-tensile tests on the struts using a dedicated setup designed for use with digital surface image correlation. As a last step, 3D image-based finite element simulation of the micro-tensile tests is carried out to enrich the analysis with the simulated mechanical fields and calibrate the constitutive behavior of the material, including ductile damage. The latter is introduced in the form of a microstructure-informed Gurson-Tvergaard-Needleman damage model where the degree of ductility of each finite element in the 3D image-based mesh is adjusted according to the local volume fraction of brittle intermetallic particles, as observed by tomography.

2. Experimental procedures

2.1. Materials

Studied materials are struts extracted from a commercial Duocel® open-cell foam with a 10 Pores Per Inch (PPI) cell size produced by ERG Aerospace Corporation. The foam is made of 6101 aluminum alloy subjected by ERG to an additional T6 precipitation hardening heat treatment (homogenization at 527 °C for 8 hours, water quench and artificial aging for 8 hours at 177 °C). The chemical composition of the alloy in the foam is listed in Table 1.

Table 1: Chemical composition of the 6101 aluminum foam in weight percent (wt.%) [25, 27]

	Cu	Mg	Mn	Si	Fe	Zn	B
Foam	0.02 : 0.03	0.19 : 0.33	0.007 : 0.01	0.27 : 0.45	0.12 : 0.33	0.008 : 0.01	0.002 : 0.03

For comparison purpose and in order to initiate the identification of the constitutive properties parameters, nine tensile samples of a wrought 6101 aluminum alloy provided by the Constellium company were also prepared. They were subjected in our lab to the same T6 heat treatment. The mechanical properties obtained at a strain rate of 10^{-3} s^{-1} with an Instron universal testing machine equipped with an optical extensometer are detailed in Table 2.

Table 2: Tensile properties of the wrought 6101 aluminum alloy in the T6 state.

Young's modulus E	Yield stress σ_0	Tensile strength	Uniform elongation	Strain to fracture A
(GPa)	(MPa)	(MPa)	(%)	(%)
72 ± 12	203 ± 3	225 ± 2	5.4 ± 0.3	17.5 ± 1.6

Nanoindentation measurements with a G200 apparatus (Agilent Technologies, USA) were carried out to assess the heterogeneity of mechanical properties in the foam. Cuboid blocks of foam (width : 15 mm) were extracted and put in a cold mounting resin holder with a 30 mm diameter. A standard metallographic polishing procedure was then used down to a final 1 μm cloth. 18 Berkovich indents were then produced in the nanoindenter on different locations in the polished foam surface, using the Continuous Stiffness Measurement (CSM) procedure [28] down to 2000 nm. The resulting hardness was measured at 1.13 $\pm$ 0.10 GPa. For comparison, the corresponding measurements performed on the T6 wrought aluminum alloy resulted in a 1.09 $\pm$ 0.03 GPa hardness.

2.2. *Tomography*

X-ray laboratory tomography [29, 30, 31] was used in this study to characterize the architecture of the extracted struts before micro-tensile testing. Samples were placed in a position from the X-ray source resulting in a 3 μm lateral voxel size. They were rotated in 720 steps between 0° and 360° and an average of three images with a 333 ms exposure was carried out at each step. The X-ray tube was operated at 80 kV acceleration voltage and 280 μA current, with a 0.1 mm copper filter to reduce beam hardening artefact. Then, a standard filtered back-projection algorithm was used to reconstruct the final 3D image. Among all struts extracted from the foam, three of them were scanned in this way.

Java programs developed in the Fiji software [32] were used to analyze the final reconstructed 3D images to quantify the variation of strut cross-section areas, sizes and barycentres of intermetallic particles, as well as the intermetallic volume fraction at each cross-section. First, the entire 3D stack was thresholded into white (255), gray (128) and black (0) 8-bits gray levels belonging respectively to intermetallic particles, aluminum and voids. A 3D rendering of a thresholded strut is as shown for example in Figure 1. The intermetallic particles correspond to α-AlFeSi (Al_8Fe_2Si) and β-AlFeSi (Al_5FeSi) precipitates mostly located in the grain boundaries [27]. The evolution of cross-section area was determined by summing the number of gray voxels in each *z* slice after filling intermetallic particles and internal microvoids in each slice. The volume fraction of intermetallic particles at each *z* slice was also calculated by dividing the number of white voxels by the total number of voxels in the filled cross-section. In addition, the equivalent diameter of intermetallic particles was determined by calculating the average diameter of each group of connected white voxels in the 3D image. The barycenter of each intermetallic particle was also computed.

Figure 1: 3D semi-transparency rendering of the reconstructed structure of strut 1 obtained by X-ray tomography. Intermetallic particles are shown in red, distributed in the gray aluminum phase.

2.3. *Micro-tensile test*

A micro-tensile machine developed by Jung et al. [14] was used to obtain the plastic behavior of the strut samples, monitored by digital image correlation (DIC). First, stochastic paint patterns were produced by subsequently spraying black and white paint droplets on the struts. Afterwards, the struts were placed in the grippers shown in Figure 2. A soft solder metal with a melting temperature lower than 100 $^\circ$C was used for that purpose, allowing to grip the sample without disturbing the existing T6 heat treatment.

Figure 2: Schematic illustration of 1) upper cross-head 2) gripper 3) solder chamber 4) fixing screw 5) testing strut.

The struts were pulled in displacement control at a rate of about 10^{-2} mm/s^{-1}. Two cameras were installed at different observation angles to measure the strain optically. It has been shown that the correlation between the images from the two cameras is independent from the strut orientation [14]. The images were taken every 0.02 mm cross-head displacement. The commercial DIC software Istra 4D®, developed by Dantec Dynamics company, was used to evaluate the local longitudinal true strain ε_z and the local lateral true strain ε_r perpendicular to the loading direction. The longitudinal stretch ratio λ_z and corresponding lateral shrinkage λ_r are defined as:

$$\lambda_z = \frac{l}{l_0} = exp(\varepsilon_z),\ \lambda_r = \frac{r}{r_0} = exp(\varepsilon_r) \tag{1}$$

where l_0 and *l* are the initial and instantaneous lengths and r_0 and *r* the initial and instantaneous radii. Assuming volume conservation of a close to cylindrical strut, the instantaneous cross-section area *A* and the true stress σ_t are defined as [14]:

$$A = A_0(\frac{r}{r_0})^2 = A_0\lambda_r^2 \tag{2}$$

$$\sigma_t = \frac{F}{A_0\lambda_r^2} \tag{3}$$

where F is the value of force read from the load cell and A_0 is the initial minimum cross-section area measured from 3D X-ray tomography images.

3. Finite element approach

A finite element model conforming to the structure and microstructure of the foam struts was build in this work. The procedure adopted to inform the damage model of a potentially brittle region due to the presence of a local cluster of intermetallic particles is detailed here.

3.1. Damage model

In this study, a standard Gurson-Tvergaard-Needleman (GTN) [33, 34, 35, 36, 37] model was used to include the mechanisms of ductile damage into the simulation, accounting for void nucleation and growth. The governing equations are expressed as:

$$\Phi\left(\sigma_{eq},\sigma_y,\sigma_H,f\right) = \left(\frac{\sigma_{eq}}{\sigma_y}\right)^2 + 2fq_1\cosh\left(\frac{3q_2\sigma_H}{2\sigma_y}\right) - \left(1+q_3f^2\right) = 0 \tag{4}$$

where Φ is yield function, q_1, q_2 and q_3 are calibrating parameters, σ_{eq} is von Mises equivalent stress, σ_y is yield stress, σ_H is hydrostatic stress, and f is the void volume fraction (VVF) in the matrix. Starting from an initial void volume fraction f_0, the total change in f including both nucleation and growth of the voids is defined as [34]:

$$\dot{f} = \dot{f}_{gr} + \dot{f}_{nucl} = (1-f)\,tr(\dot{\boldsymbol{\varepsilon}}^{pl}) + \frac{f_N}{s_N\sqrt{2\pi}}\exp\left[-\frac{1}{2}\left(\frac{\varepsilon_{eq}^{pl}-\varepsilon_N}{s_N}\right)^2\right]\dot{\varepsilon}_{eq}^{pl} \tag{5}$$

where $\dot{f}_{gr}$ is the void growth rate which is based on mass conservation and directly proportional to the hydrostatic component of the plastic strain rate tensor $\dot{\boldsymbol{\varepsilon}}^{pl}$ and ε_{eq}^{pl} is the equivalent plastic strain. $\dot{f}_{nucl}$ is the contribution of nucleation. ε_N and s_N are the mean value and standard deviation of the nucleation distribution with strain, respectively. f_N is the volume fraction of the nucleated voids.

The work hardening behavior of the non porous aluminum was defined as the following power law [38]:

$$\frac{\sigma_y}{\sigma_0} = (\frac{\sigma_y}{\sigma_0} + \frac{3G}{\sigma_0}\varepsilon^{pl})^N \quad (6)$$

where σ_0 is the initial yield stress, N is the hardening exponent and $G = \frac{E}{2(1+\nu)}$ the elastic shear modulus.

3.2. Microstructure mesh and boundary conditions

In order to build a FE model conforming to the microstructure, the 3D X-ray images of the struts were analyzed with the commercial Avizo® 9 software [39]. First, a surface mesh corresponding to the exterior boundary of the solid phase was produced with 3-node triangles. Then, the obtained triangles were simplified step by step and remeshed to reduce their number while preserving a proper description of the surface with close to equilateral triangles. Finally, the solid volume was meshed with tetrahedral elements using the Gmsh software [40] and exported to the Abaqus® file format. The average characteristic element size L was chosen between 120 and 180 μm. In the case of strut 1, two additional meshes with a finer element size were also generated to check for the convergence of simulation results. The number of nodes and elements of the different volumes are detailed in Table 3.

Table 3: Number of nodes and elements of the investigated volume meshes. The influence of element size is investigated on strut 1.

	Characteristic element size L(μm)	Number of nodes	Number of elements
Strut 1	60-120	10110	65973
Strut 1	90-150	4367	28421
Strut 1	120-180	2366	15338
Strut 2	120-180	3443	22279
Strut 3	120-180	2672	17243

In order to include the presence of intermetallic particles in the generated FE meshes, the volume fraction of intermetallic particles f_{IM} in each tetrahedron of volume meshes was determined using a dedicated Python script described in [23, 41]. It considers the coordinates of white (intermetallics) and gray (aluminum) voxels of the 3D segmented images and calculates the ratio of white voxels to the total number of voxels located inside the volume of each tetrahedron. Afterwards, the tetrahedra were tagged and stored in different classes according to their values of f_{IM}, as illustrated in Figure 3. This was then used to attribute different mechanical properties to each element according to the local level of f_{IM}, as detailed below.

Figure 3: Distribution of intermetallics volume fraction f_{IM} in the tetrahedra of the three tested struts (characteristic element size L = 120- 180 μm).

The boundary conditions applied in the simulations were meant to reproduce a perfect uniaxial tensile loading of the struts, in the absence of a detailed 3D full-field measurement of the displacement field in the experiments. As a matter of fact, the set of 3D boundary conditions leading to the observed 2D DIC-based deviation from uniaxial loading is not unique. The vertical displacement u_z of the top surface of the struts was imposed while maintaining $u_z = 0$ at the bottom surface. Moreover, the global axial twisting about *z*-axis of the specimens was prevented by blocking the rotation of both top and bottom surfaces. The simulations were run with the Abaqus®-Standard solver under quasi-static conditions [38].

An additional concern for the definition of a macroscopic tensile stress as in the experiment (section 2.3) is the definition of a proper cross section area *A*. The minimum cross-section area at each time step in the simulations was evaluated using a dedicated Python script. The code splits the deformed mesh into *n* slices (*n* depending on the characteristic element size) perpendicular to the tensile direction and determines the minimum cross-section area in the current time step. The later is used to define the macroscopic true stress $\sigma_t = \frac{F}{A}$ and true strain $\varepsilon_t = ln(\frac{A_0}{A})$.

3.3. Composite flow curves and model parameters

Each tetrahedron in the FE mesh is considered in this work as a composite material with a given volume fraction of intermetallics f_{IM} in an aluminum matrix. In order to compute the elastic properties and flow curves of the different equivalent composites with increasing f_{IM}, the present work relies on axisymmetric cell calculation [23], assuming isotropic elastic behavior of the particles (E_{IM} = 160 GPa, $\nu_{IM} = 0.33$ [12]) and J_2 elastoplastic behavior of the aluminum matrix (σ_0 = 288 MPa, $N = 0.052$ in Equation 6). The composite behavior is then transferred to the GTN damage model of section 3.1 with q_1 = 1.5, q_2 = 1.0 and q_3 = 2.25 [36] and $f_0 = 0$. The model parameters depending on the increasing volume fraction of intermetallics are detailed in Table 4. The reader is referred to [23] for the details of the procedure. Figure 4 illustrates the average behavior of the different composites with increasing f_{IM} using the GTN damage model. Table 4 and Figure 4 reproduce the transition to a harder behavior with lower ductility when the intermetallic fraction increases in the composite.

Table 4: Young's modulus *E*, hardening parameters (Equation 6) and GTN nucleation parameters (Equation 5) for the equivalent composites with increasing volume fractions f_{IM} of intermetallic particles.

f_{IM}	E	σ_0	N	f_N	ε_N	s_N
	(GPa)	(MPa)				
0.0	70	288	0.052	0.04	0.18	0.06
0.1	76	298	0.045	0.04	0.16	0.05
0.2	83	314	0.037	0.04	0.13	0.04
0.3	90	339	0.030	0.04	0.10	0.03
0.4	98	379	0.022	0.04	0.08	0.03

0.5	106	461	0.015	0.04	0.05	0.02
0.6	115	549	0.007	0.04	0.03	0.01

Figure 4: Simulated tensile curves of the different composites with increasing f_{IM} using the GTN damage model.

4. Results

4.1. Experimental results

Figure 5: a) Experimental stress-strain curves for the three struts. b) DIC fields of the first principal Lagrange strain in the struts at the last point before fracture, arrows pointing to the imminent location of fracture.

Figure 5.a shows the experimental tensile curves for the three investigated struts. They were obtained from the post-treatment of micro-tensile tests under DIC described in section 2.3. The inset highlights the elastic regime of the curves. One can note the dispersion in stiffness, strength, hardening and ductility. It arises from the non standardized (not homogeneous) geometry and gripping of the samples on top of the heterogeneous microstructure inside and between the samples.

Figure 5.b shows the surface fields of the first (maximum) principal component of the Lagrange strain obtained by DIC for the different struts, just before the advent of the final fracture crack. The arrows point at the location of the imminent final crack. These maps illustrate the heterogeneity strain, even if observed here only at the surface.

In order to better understand the causes for such heterogeneity and their consequences on fracture, two contributions are analyzed further in this study: (i) the effect of an irregular cross-section area along the height of the struts and (ii) the effect of brittle intermetallic particles. Previous studies [12, 22] postulated indeed that local clusters of brittle intermetallic particles might constitute preferential zones for damage and fracture in metallic foams. The initial tomography scans of the samples allow to assess both the irregular outer shape of the struts and the heterogeneity of particle distribution within the struts.

Figure 6: Variations of the cross-section areas along the struts.

Figure 6 depicts the evolution of the initial cross section area along the height (z-direction) of the struts as obtained from the 3D tomography scans. The dashed lines highlight the observed locations of fracture. As a matter of fact, one would expect easier strain localization and damage development where the local cross-section area is minimum, inducing a higher local true stress.

Fracture takes place indeed at the location of the minimum cross-section area in the case of strut 3. This is also almost, but not exactly, the case for strut 1. Strut 2 presents however a rather homogeneous cross-section area, impeding the analysis of fracture location based on that sole criterion.

In the analyzed struts, the average equivalent diameter of the intermetallic particles is 8 μm, the biggest one reaching 104 μm. Figure 1, section 2.2, illustrates that the particles are much bigger in the strut ends than in the middle. For comparison purpose, smaller particles with a more homogeneous distribution (average size 4 μm, maximum size 5 μm) were measured in the wrought 6101 aluminum alloy using the same procedure.

Figure 7 shows the evolution of the biggest particle size as well as of the local particle volume fraction at each *z* slice of the investigated struts. The location of fracture obtained in the micro-tensile tests is indicated using dashed lines as in Figure 6. These plots confirm the heterogeneity of particle distribution, both in size and in volume fraction. The experimental fracture location corresponds to a local maximum in particle diameter and in particle volume fraction for both struts 1 and 2. This appears as a decisive factor for strut 2 in the absence of significant cross-section variation. It might also contribute to the small shift of fracture location away from the minimum cross-section in the case of strut 1. In strut 3 however, neither the particle size nor the volume fraction correlates with the fracture zone, while the local reduction in cross-section area did in Figure 6.

Figure 7: Equivalent diameter of the biggest particles (a, c, e) and intermetallic volume fraction (b, d, f) at each *z* slice along the length of struts 1 (a, b), strut 2 (c, d) and strut 3 (e, f). Dashed lines correspond to fracture location.

Figures 6 and 7 together illustrate the competition between a localization of damage and fracture driven by the structure (external shape of the struts) or driven by the microstructure (influence of the intermetallic particles). The particular example of these 3 struts tend to confirm the primary influence of the structure [23] and second order effect of microstructure (only where structure variations are not discriminant).

4.2. Simulation results

The modeling procedure adopted in this work was designed to catch the competition between structure and microstructure discussed above. This relies on the ability to build an image-based FE model conforming to the reconstructed tomography volumes (structure sensitive) and to inform each finite element of the mesh of the local fraction of intermetallic particles in order to drive its constitutive behavior (microstructure sensitive).

A first concern in the procedure might be the dependence of simulated results on the chosen element size (see Table 3). Figure 8.a-c shows the effect of mesh refinement on the local level of intermetallic volume fraction f_{IM}, determining the local constitutive behavior. The chosen element size of 120-180 μm (used in the remaining of this study) allows a reasonable description of the intermetallic heterogeneity at low computational cost. Figure 8.d confirms that the investigated element sizes do not significantly affect the global stress-strain curves of strut 1, always lying rather close to the experimental one at least in the major part of the deformation (some discrepancies can be observed at high strain). The inset in Figure 8.d shows that this remains valid in the elastic regime.

Figure 8: Mesh size sensitivity. Intermetallic fraction f_{IM} in the volume mesh of strut 1 with a characteristic element size of (a) $L = 120 - 180$ μm, (b) $L = 90 - 150$ μm and (c) $L = 60 - 120$ μm. d) Resulting stress-strain curves compared to the experimental one.

Figure 9.a investigates the effect of the local constitutive behavior on the stress-strain curve of strut 1. The red solid line corresponds to the microstructure-sensitive model with GTN damage introduced above. Three levels of simplification of the model were investigated here: (i) considering the model with GTN damage, but with the average fraction of intermetallics distributed homogeneously in the sample (blue solid line), (ii) considering the heterogeneous distribution of intermetallics, but without GTN damage (red dashed line) and (iii) considering the average homogeneous distribution of intermetallics without GTN damage (blue dashed line). The effect of the heterogeneous distribution of particles is highlighted by comparing the blue and red curves. This effect turns out to be very small when looking at such macroscopic tensile response only. The effect of porous plasticity and damage is highlighted by comparing the dashed lines with the continuous lines. Damage induces a significant softening for both types of particle distribution (homogeneous and heterogeneous), especially in the last part of the tensile curve. One can note that the elastic regime highlighted in the inset of Figure 9.a is barely affected by the heterogeneous distribution of particles, as one could expect from their small overall volume fraction.

Figure 9: Simulated stress-strain curves: a) influence of the material model in strut 1, b) comparison of the three specimens with the heterogeneous GTN model, recalling the experimental curves of Figure 5 in gray.

Figure 9.b shows the simulated tensile curves of the three struts, using the microstructure-sensitive GTN model. The model predicts a significant difference in ductility between the three struts, but an identical tensile strength around 320 MPa and a similar stiffness as highlighted in the inset. This is in contrast with the experimental tensile curves of Figure 5 (recalled in gray in Figure 9.b) with tensile strength levels ranging from 325 to 375 MPa and significant difference in stiffness. It appears clearly here that the sole variations of shape and particle distribution (both accounted for in the simulations), assuming uniaxial tension, are not sufficient to explain such scattering in strut strength and stiffness.

Figure 10: Contour plots of von Mises stress at ε = 0.24 for strut 1: (a) homogeneous and (b) heterogeneous GTN models. Corresponding contour plots of void volume fraction *f*: (c) homogeneous and (d) heterogeneous GTN models.

Figures 10 shows the von Mises stress distribution and the void volume fraction at a strain of 0.24 in strut 1, for both homogeneous and heterogeneous GTN models. Stress distribution in the strut is rather similar with the two types of models, as illustrated in Figures 10.a and 10.b. Void volume fraction in Figures 10.c and 10.d shows a slightly wider expansion in the case of the heterogeneous GTN model. This is due to the presence of intermetallic particles below the surface, contributing to the faster evolution of void volume fraction.

Figure 11: Vertical positions of the fracture planes for the three struts, in the experiment, in the homogeneous and in the heterogeneous GTN models.

In the FE simulations, one considers the predicted location of fracture as the cross-section at the position *z* containing the element with the maximum void volume fraction. These locations of fracture are illustrated in Figure 11 for the three struts and for the two types of GTN models (homogeneous and heterogeneous), next to the experimental observation from the micro-tensile tests. One can note here that the predicted location of fracture is always slightly closer to the experimental position with the heterogeneous GTN model rather than with the homogeneous one. However, the homogeneous model provides already a fairly good estimation of the location of fracture, highlighting again the first order effect of structure and geometry.

5. Discussion and perspectives

The presented work investigated the behavior of individual struts extracted from an open-cell foam and subjected to micro-tensile tests as well as to 3D image-based FE simulations of the tests. The modeling procedure was shown to be both structure-sensitive (following the actual geometry of the samples) and microstructure-sensitive (accounting for the heterogeneity of distribution in intermetallic particles). It succeeds in a rather close prediction of fracture location in the struts, but fails at reproducing the dispersion in strength measured experimentally. As a matter of fact, such dispersion of strength measures in single-strut experiments has been observed in previous studies ([13, 14]), along with potential discrepancies between microsample-based measures and the corresponding ones using standardized experiments on bulk alloys [42].

A first point raised in the present work pertains to the actual boundary conditions in the micro-tensile tests and in the simulations. Despite great care in the preparation and mounting of the (millimetric) struts in the micro-tensile machine, the degree of deviation of the applied load from a pure uniaxial one was not controlled in the experiment. This might contribute to the discrepancy between the stiffness and strength levels measured on the different struts and the predictions with the present model, assuming a uniaxial load. Beyond modifications of the test setup and mounting procedure, one alternative solution would consist in applying non uniform displacements at the model boundaries. This would be best achieved using full-field measurements of the displacement fields in the experiment, as obtained for example by Digital Volume Correlation (DVC). This will be the topic of future work based on in situ tensile testing in the tomograph.

A second point of discussion is related to the assumed isotropic behavior of the materials in the model, from the aluminum matrix to different composites with increasing fraction of intermetallic particles. Starting with the aluminum matrix, it is likely that the individual behavior of the micro-samples is in fact quite sensitive to the crystallographic orientation of the couple of face-centered-cubic (FCC) grains constituting each strut [27]. Assuming for example a critical resolved shear stress for dislocation glide of 100 MPa in a given crystal and usual Taylor factors in tension ranging from 2.5 to 3.5 for the sake of simplicity, one would expect a yield strength varying from 250 to 350 MPa depending on crystal orientation. This is in contrast to the averaged behavior of a usual bulk tensile sample made of thousands of grains. Crystal plasticity FE modeling based on measured crystallographic orientation fields [43] would be the natural perspective here. They require however complex experimental setups such as Diffraction Contrast Tomography [26] in order to map grain orientations non destructively in 3D. This is doable but out of the scope of the present study.

Another source of anisotropy at the local level arises from the actual complex shape and arrangement of the intermetallic particles in the aluminum matrix. This is indeed likely to affect not only the strength, but also the sequence of damage mechanisms leading to fracture from nucleation of cavities (by particle debonding or fracture [44]) to growth and coalescence [45]. The GTN model adopted here constitutes a computationally cheap approach of the sequence of ductile damage, which presents the advantage of being applicable at higher scale under the same modeling framework. This was carried out for example at the scale of the foam structure in [23] or with an additive manufacturing lattice structure in [41]. However, both the phenomenological description (Gaussian distribution) of cavity nucleation in the GTN model and the underlying assumption of spherical cavities might be the topic of improvement in future work.

6. Conclusion

Within the scope of this study, the tensile fracture of struts extracted from an open-cell Al-foam was studied using micro-tensile tests and FE approaches. 3D image-based FE meshes of the studied struts were built based on X-ray tomography scans. A microstructure-sensitive model was used, informing each tetrahedron in the mesh of the local intermetallic volume fraction and adapting the yield stress and ductility accordingly within the framework of a GTN porous plasticity model.

The image-based, microstructure-sensitive FE model succeeds in predicting fracture location precisely in the struts but fails at reproducing the dispersion in strength measured in the single-strut experiments. Both experimental and numerical results tend to confirm the primary influence of structure and geometry on the mechanical behavior of the struts as well as the second order influence of microstructure understood here in terms of intermetallic particle distribution. Other important concerns to be integrated in future work will include 3D full-field measurements of the displacement fields as well as the crystallographic orientation of the couple of grains in the struts.

Acknowledgment

The authors would like to thank P. Lorenzino and the Constellium company for providing the bulk aluminum samples as well as J. Adrien and J. Lachambre for their help and advises on X-ray tomography.

Data availability

The raw/processed data required to reproduce these findings cannot be shared at this time as the data also forms part of an ongoing study.

References

[1] M. F. Ashby, Metal foams: A design guide, Butterworth-Heinemann, Boston, 2000.

[2] Y. Amani, A. Takahashi, P. Chantrenne, S. Maruyama, S. Dancette, E. Maire, Thermal conductivity of highly porous metal foams: Experimental and image based finite element analysis, International Journal of Heat and Mass Transfer 122 (2018) 1–10. doi:10.1016/j.ijheatmasstransfer.2018.01.050.

[3] L. J. Gibson, M. F. Ashby, Cellular solids: Structure and properties, 2nd Edition, Cambridge solid state science series, Cambridge Univ. Press, Cambridge [u.a.], 2010.

[4] M. Scheffler, Cellular ceramics: Structure, manufacturing, properties and applications, WILEY-VCH, Weinheim, 2006.

[5] A. Harte, The fatigue strength of sandwich beams with an aluminium alloy foam core, Int. J. Fatigue 23 (6) (2001) 499–507. doi:10.1016/S0142-1123(01)00012-3.

[6] J. Banhart, Manufacture, characterisation and application of cellular metals and metal foams, Prog. Mater. Sci. 46 (6) (2001) 559–632. doi:10.1016/S0079-6425(00)00002-5.

[7] M. A. Hasan, A. Kim, H. J. Lee, Measuring the cell wall mechanical properties of Al-alloy foams using the nanoindentation method, Composite Structures 83 (2) (2008) 180–188. doi:10.1016/j.compstruct.2007.04.016.

[8] O. Jiroušek, I. Jandejsek, D. Vavřík, Evaluation of strain field in microstructures using micro-CT and digital volume correlation, Journal of Instrumentation 6 (01) (2011) C01039–C01039. doi:10.1088/1748-0221/6/01/C01039.

[9] J. Olofsson, I. L. Svensson, P. Lava, D. Debruyne, Characterisation and investigation of local variations in mechanical behaviour in cast aluminium using gradient solidification, digital image correlation and finite element simulation, Mater. Des. (1980-2015) 56 (2014) 755–762. doi:10.1016/j.matdes.2013.12.036.

[10] A. E. Markaki, T. W. Clyne, The effect of cell wall microstructure on the deformation and fracture of aluminium-based foams, Acta Materialia 49 (9) (2001) 1677–1686. doi:10.1016/S1359-6454(01)00072-6.

[11] A. Jung, Z. Chen, J. Schmauch, C. Motz, S. Diebels, Micromechanical characterisation of ni/al hybrid foams by nano- and microindentation coupled with ebsd, Acta Materialia 102 (2016) 38 – 48. doi:https://doi.org/10.1016/j.actamat.2015.09.018.

[12] C. Petit, E. Maire, S. Meille, J. Adrien, Two-scale study of the fracture of an aluminum foam by X-ray tomography and finite element modeling, Materials & Design 120 (2017) 117–127. doi:10.1016/j.matdes.2017.02.009.

[13] J. Zhou, S. Allameh, W. O. Soboyejo, Microscale testing of the strut in open cell aluminum foams, J. Mater. Sci. 40 (2) (2005) 429–439. doi:10.1007/s10853-005-6100-8.

[14] A. Jung, M. Wocker, Z. Chen, H. Seibert, Microtensile testing of open-cell metal foams — Experimental setup, micromechanical properties, Mater. Des. 88 (2015) 1021–1030. doi:10.1016/j.matdes.2015.09.091.

[15] A. Jung, J. Luksch, S. Diebels, F. Schäfer, C. Motz, In-situ and ex-situ microtensile testing of individual struts of al foams and ni/al hybrid foams, Mater. Des. 153 (2018) 104 – 119. doi:https://doi.org/10.1016/j.matdes.2018.04.075.

[16] H. Bart-Smith, A. F. Bastawros, D. R. Mumm, A. G. Evans, D. J. Sypeck, H. N. G. Wadley, Compressive deformation and yielding mechanisms in cellular Al alloys determined using X-ray tomography and surface strain mapping, Acta Mater. 46 (10) (1998) 3583–3592. doi:10.1016/S1359-6454(98)00025-1.

[17] H. Toda, T. Kobayashi, M. Niinomi, T. Ohgaki, M. Kobayashi, N. Kuroda, T. Akahori, K. Uesugi, K. Makii, Y. Aruga, Quantitative assessment of microstructure and its effects on compression behavior of aluminum foams via high-resolution synchrotron X-ray tomography, Metallurgical and Materials Transactions A 37 (4) (2006) 1211–1219. doi:10.1007/s11661-006-1072-0.

[18] I. Jeon, T. Asahina, K. J. Kang, S. Im, T. Lu, Finite element simulation of the plastic collapse of closed-cell aluminum foams with X-ray computed tomography, Mechanics of Materials 42 (3) (2010) 227–236. doi:10.1016/j.mechmat.2010.01.003.

[19] C. Betts, D. Balint, J. Lin, In-situ micro-tensile testing and X-ray micro-tomography based FE modeling of open-cell metal Foam struts and sandwich panels, Procedia Mater. Sci. 4

(2014) 197–202. doi:10.1016/j.mspro.2014.07.595.

[20] O. Caty, E. Maire, S. Youssef, R. Bouchet, Modeling the properties of closed-cell cellular materials from tomography images using finite shell elements, Acta Mater. 56 (19) (2008) 5524–5534. doi:10.1016/j.actamat.2008.07.023.

[21] S. Youssef, E. Maire, R. Gaertner, Finite element modelling of the actual structure of cellular materials determined by x-ray tomography, Acta Mater. 53 (3) (2005) 719–730. doi:10.1016/j.actamat.2004.10.024.

[22] T. Zhang, E. Maire, J. Adrien, P. R. Onck, L. Salvo, Local tomography study of the fracture of an ERG metal foam, Adv. Eng. Mater. 15 (8) (2013) 767–772. doi:10.1002/adem.201300004.

[23] Y. Amani, S. Dancette, E. Maire, J. Adrien, J. Lachambre, Two-Scale Tomography Based Finite Element Modeling of Plasticity and Damage in Aluminum Foams, Materials 11 (10) (2018) 1984. doi:10.3390/ma11101984.

[24] Y. Brechet, J. Embury, Architectured materials: Expanding materials space, Scripta Materialia 68 (1) (2013) 1–3. doi:10.1016/j.scriptamat.2012.07.038.

[25] J. Zhou, C. Mercer, W. O. Soboyejo, An investigation of the microstructure and strength of open-cell 6101 aluminum foams, Metall. Mater. Trans. A 33 (5) (2002) 1413–1427. doi:10.1007/s11661-002-0065-x.

[26] W. Ludwig, P. Reischig, A. King, M. Herbig, E. M. Lauridsen, G. Johnson, T. J. Marrow, J. Y. Buffière, Three-dimensional grain mapping by x-ray diffraction contrast tomography and the use of Friedel pairs in diffraction data analysis, Review of Scientific Instruments 80 (3) (2009) 033905. doi:10.1063/1.3100200.

[27] E. Amsterdam, P. R. Onck, J. T. M. de Hosson, Fracture and microstructure of open cell aluminum foam, J. Mater. Sci. 40 (22) (2005) 5813–5819. doi:10.1007/s10853-005-4995-8.

[28] J. Hay, P. Agee, E. Herbert, Continuous stiffness measurement during instrumented indentation testing, Exp. Tech. 34 (3) (2010) 86–94. doi:10.1111/j.1747-1567.2010.00618.x.

[29] E. Maire, X-ray tomography applied to the characterization of highly porous materials, Annu. Rev. Mater. Res. 42 (2012) 163–178. doi:10.1146/annurev-matsci-070511-155106.

[30] E. Maire, P. J. Withers, Quantitative X-ray tomography, Int. Mater. Rev. 59 (1) (2014) 1–43. doi:10.1179/1743280413Y.0000000023.

[31] G. T. Herman, Fundamentals of computerized tomography: Image reconstruction from projections, Springer Science & Business Media, 2009.

[32] J. Schindelin, I. Arganda-Carreras, E. Frise, V. Kaynig, M. Longair, T. Pietzsch, S. Preibisch, C. Rueden, S. Saalfeld, B. Schmid, et al., Fiji: an open-source platform for biological-image analysis, Nature methods 9 (7) (2012) 676.

[33] A. L. Gurson, Continuum theory of ductile rupture by void nucleation and growth: Part I—Yield criteria and flow rules for porous ductile media, J. Eng. Mater. Technol. 99 (1) (1977) 2. doi:10.1115/1.3443401.

[34] C. C. Chu, A. Needleman, Void nucleation effects in biaxially stretched sheets, J. Eng. Mater. Technol. 102 (3) (1980) 249. doi:10.1115/1.3224807.

[35] V. Tvergaard, Influence of voids on shear band instabilities under plane strain conditions, Int. J. Fract. 17 (4) (1981) 389–407. doi:10.1007/BF00036191.

[36] V. Tvergaard, On localization in ductile materials containing spherical voids, Int. J. Fract. 18 (4) (1982) 237–252. doi:10.1007/BF00015686.

[37] V. Tvergaard, A. Needleman, Analysis of the cup-cone fracture in a round tensile bar, Acta Metall. 32 (1) (1984) 157–169. doi:10.1016/0001-6160(84)90213-X.

[38] Abaqus version 6.13 documentation collection (2013).

[39] Avizo® 9 user’s guide (2016).

[40] C. Geuzaine, J. F. Remacle, Gmsh: A 3-D finite element mesh generator with

built-in pre- and post-processing facilities, Int. J. Numer. Meth. Eng 79 (11) (2009) 1309–1331. doi:10.1002/nme.2579.

[41] Y. Amani, S. Dancette, P. Delroisse, A. Simar, E. Maire, Compression behavior of lattice structures produced by selective laser melting: X-ray tomography based experimental and finite element approaches, Acta Materialia 159 (2018) 395–407. doi:10.1016/j.actamat.2018.08.030.

[42] M. Hakamada, M. Mabuchi, Mechanical strength of nanoporous gold fabricated by dealloying, Scr. Mater. 56 (11) (2007) 1003–1006. doi:10.1016/j.scriptamat.2007.01.046.

[43] S. Dancette, A. Browet, G. Martin, M. Willemet, L. Delannay, Automatic processing of an orientation map into a finite element mesh that conforms to grain boundaries, Modell. Simul. Mater. Sci. Eng. 24 (5) (2016) 055014.

[44] A. Ferre, S. Dancette, E. Maire, Damage characterisation in aluminium matrix composites reinforced with amorphous metal inclusions, Mater. Sci. Technol. 31 (5) (2015) 579–586. doi:10.1179/1743284714Y.0000000619.

[45] C. I. A. Thomson, M. J. Worswick, A. K. Pilkey, D. J. Lloyd, G. Burger, Modeling void nucleation and growth within periodic clusters of particles, J. Mech. Phys. Solids 47 (1) (1998) 1–26. doi:10.1016/S0022-5096(98)00088-X.

Declaration of interests

X The authors declare that they have no known competing financial interests or personal relationships that could have appeared to influence the work reported in this paper.

☐The authors declare the following financial interests/personal relationships which may be considered as potential competing interests:

Highlights

- Individual struts extracted from an open-cell aluminum are investigated in tension.
- Effect of structure and shape as well as microstructure (intermetallic particles) is investigated by
- X-ray tomography and Digital Image Correlation.
- A microstructure-informed, image-based finite element model is built to predict fracture.
- Model and experiments highlight the first order effect of structure and shape on the plastic flow and fracture of the struts.

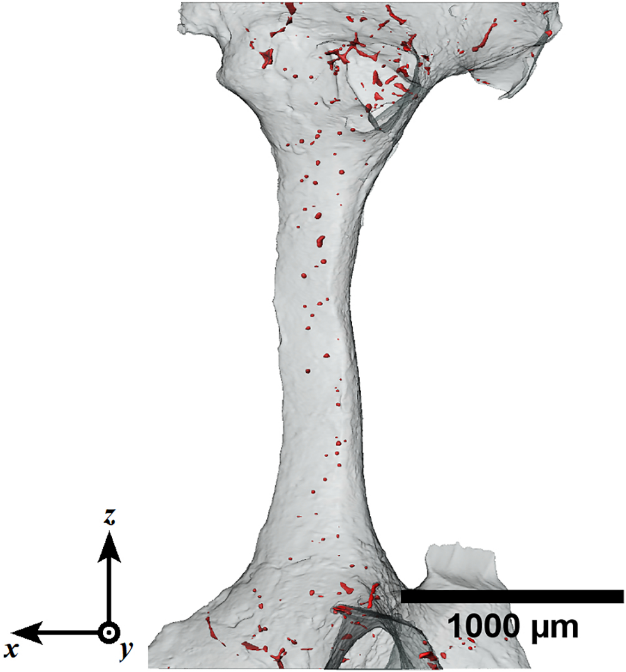

Figure 1

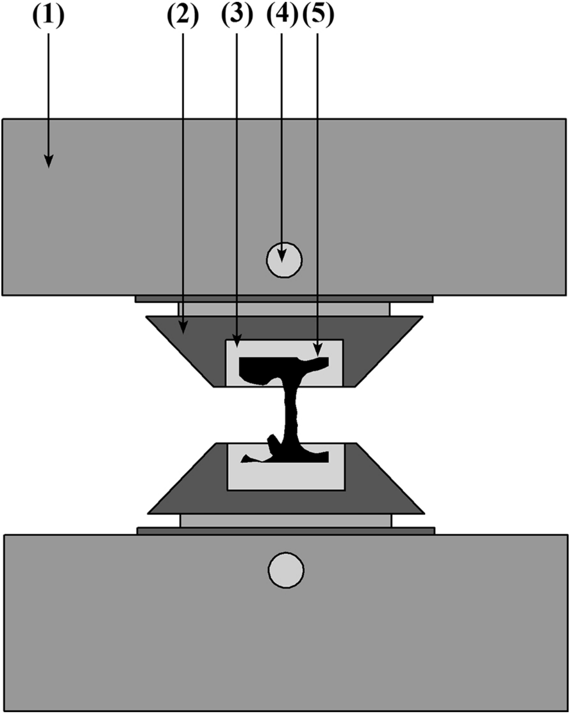

Figure 2

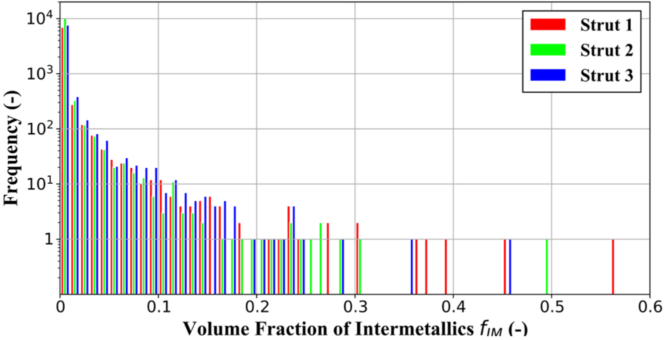
Strut 1
Strut 2
Strut 3
Frequency (-)
Volume Fraction of Intermetallics f_{IM} (-)
10^4
10^3
10^2
10^1
1
0
0.1
0.2
0.3
0.4
0.5
0.6

Figure 3

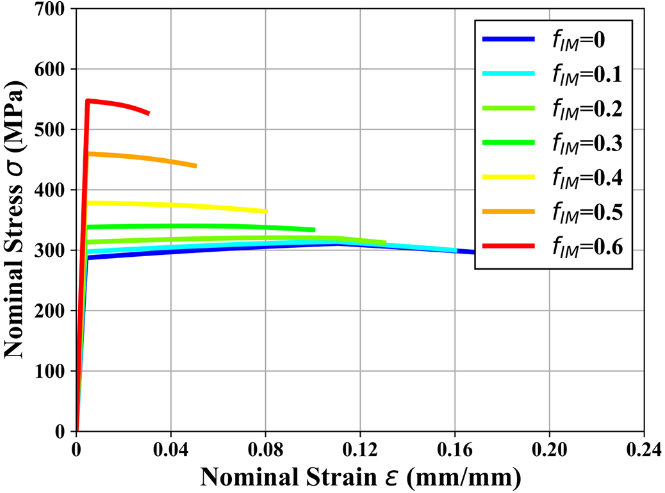

Nominal Stress σ (MPa)
Nominal Strain ε (mm/mm)
0
100
200
300
400
500
600
700
0
0.04
0.08
0.12
0.16
0.20
0.24
f_{IM}=0
f_{IM}=0.1
f_{IM}=0.2
f_{IM}=0.3
f_{IM}=0.4
f_{IM}=0.5
f_{IM}=0.6

Figure 4

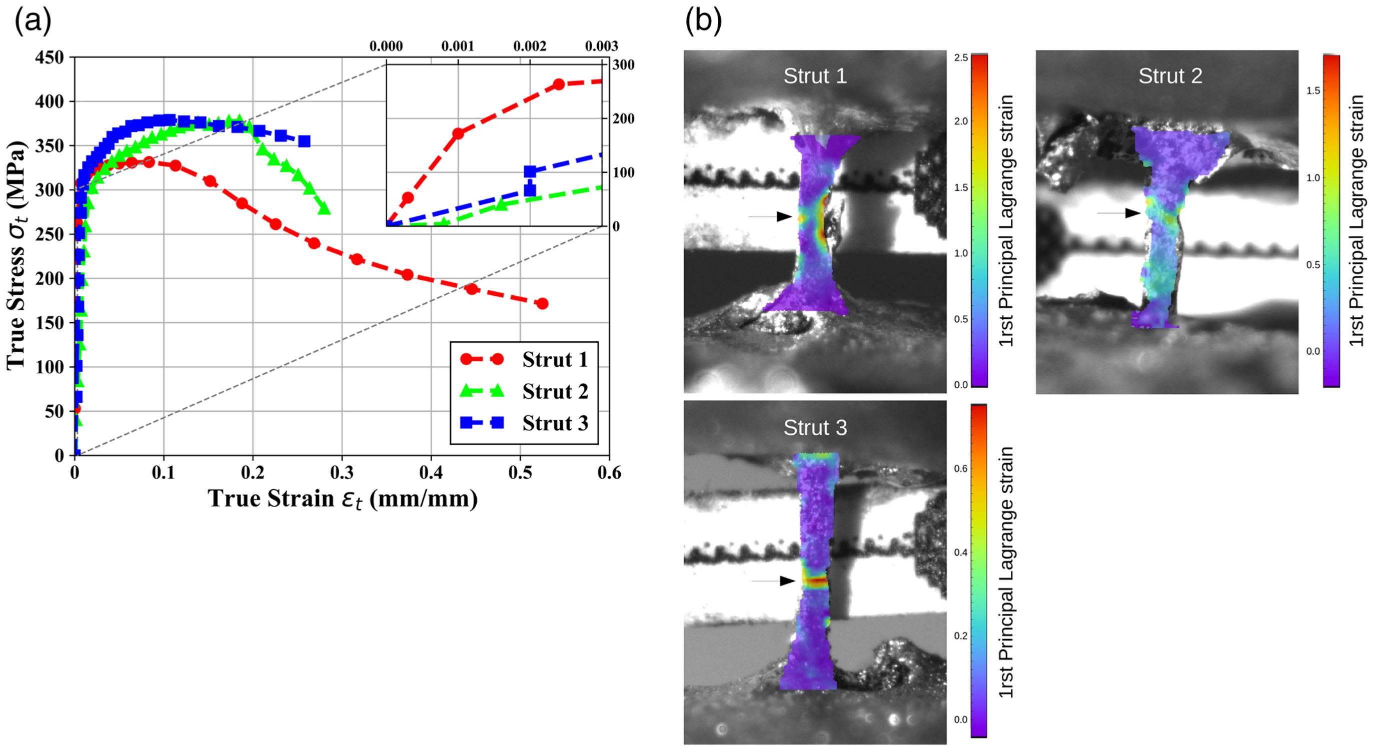
(a)
(b)
True Stress σ_t (MPa)
True Strain ε_t (mm/mm)
Strut 1
Strut 2
Strut 3
1rst Principal Lagrange strain

Figure 5

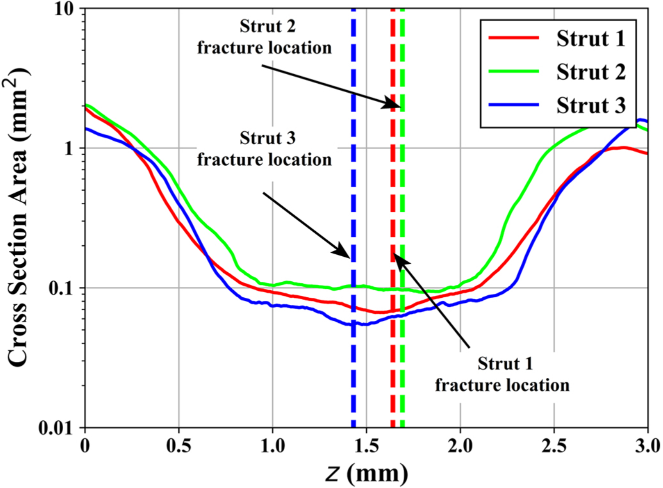
Strut 2
fracture location
Strut 3
fracture location
Strut 1
fracture location
Strut 1
Strut 2
Strut 3
Cross Section Area (mm²)
10
1
0.1
0.01
0
0.5
1.0
1.5
2.0
2.5
3.0
Z (mm)

Figure 6

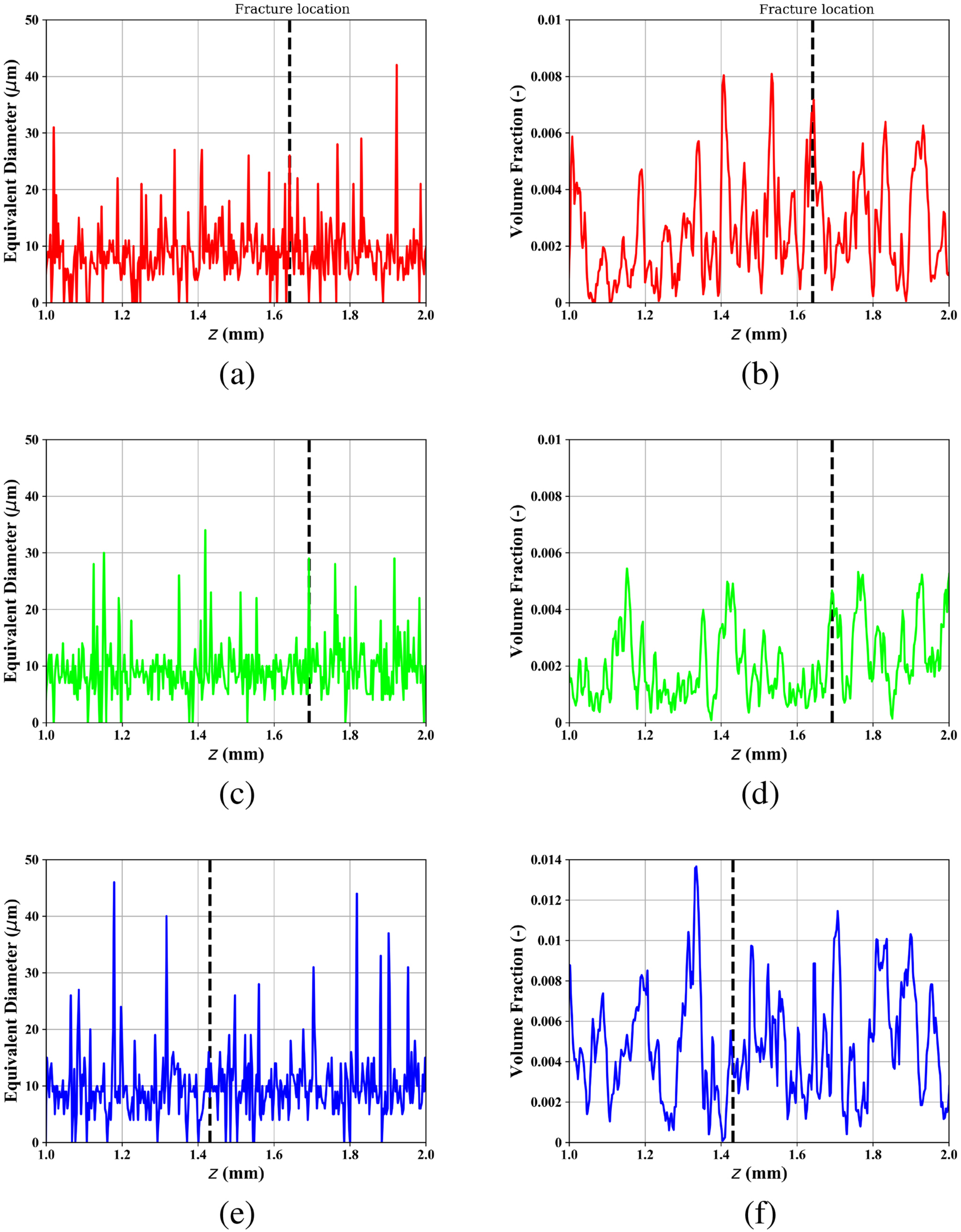
Fracture location
Equivalent Diameter (μm)
z (mm)
(a)
Fracture location
Volume Fraction (-)
z (mm)
(b)
Equivalent Diameter (μm)
z (mm)
(c)
Volume Fraction (-)
z (mm)
(d)
Equivalent Diameter (μm)
z (mm)
(e)
Volume Fraction (-)
z (mm)
(f)

Figure 7

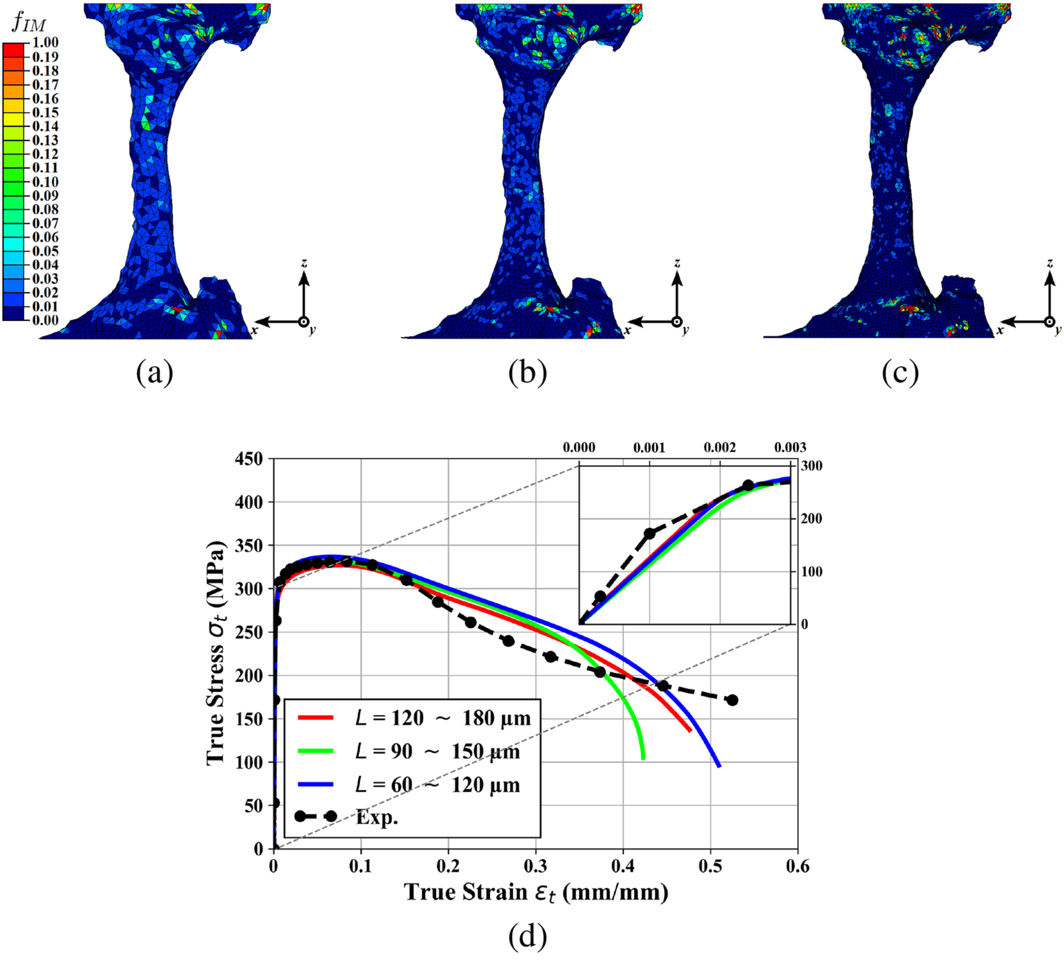

f_{IM}
1.00
0.19
0.18
0.17
0.16
0.15
0.14
0.13
0.12
0.11
0.10
0.09
0.08
0.07
0.06
0.05
0.04
0.03
0.02
0.01
0.00
z
x
y
(a)
(b)
(c)
True Stress σ_t (MPa)
True Strain ε_t (mm/mm)
L = 120 ~ 180 μm
L = 90 ~ 150 μm
L = 60 ~ 120 μm
Exp.
0
50
100
150
200
250
300
350
400
450
0.1
0.2
0.3
0.4
0.5
0.6
0.000
0.001
0.002
0.003
(d)

Figure 8

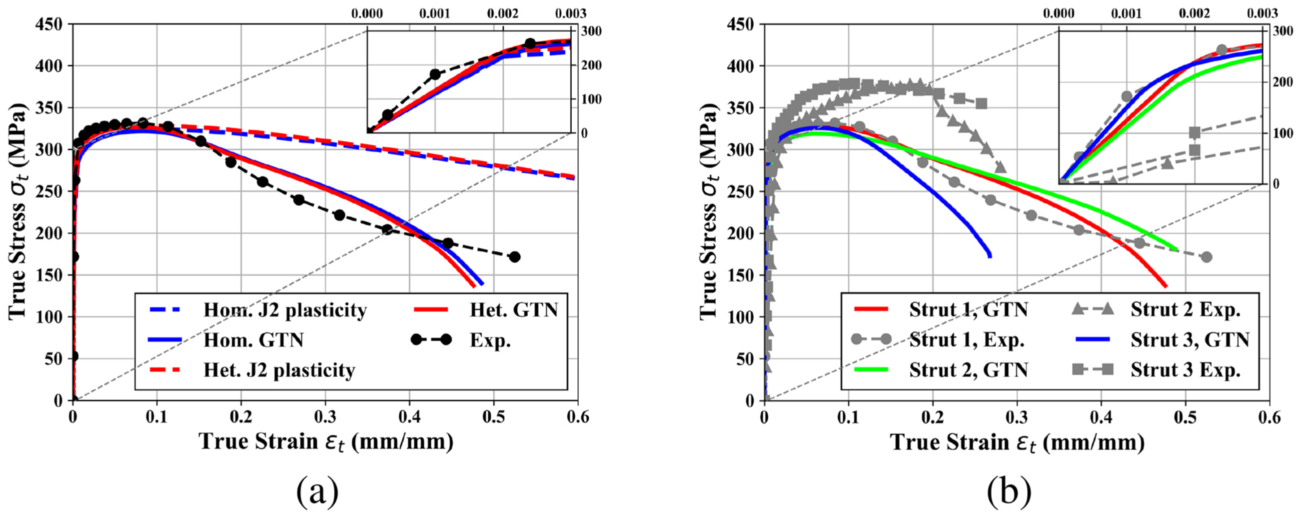

True Stress σ_t (MPa)
True Strain ε_t (mm/mm)
Hom. J2 plasticity
Hom. GTN
Het. J2 plasticity
Het. GTN
Exp.
(a)
Strut 1, GTN
Strut 1, Exp.
Strut 2, GTN
Strut 2 Exp.
Strut 3, GTN
Strut 3 Exp.
(b)

Figure 9

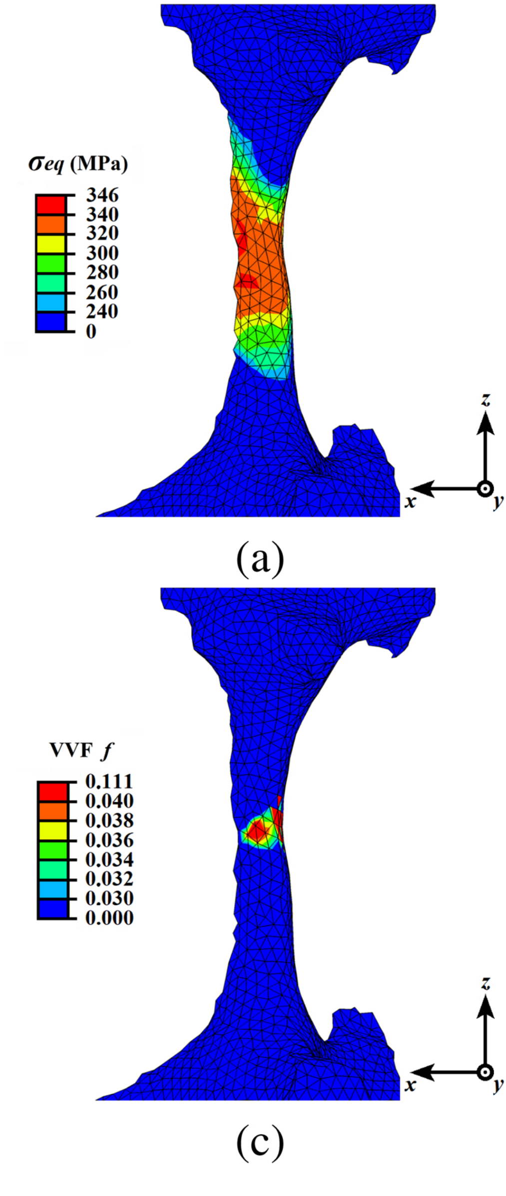

σeq (MPa)
346
340
320
300
280
260
240
0
z
x
y
(a)
σeq (MPa)
364
340
320
300
280
260
240
0
z
x
y
(b)
VVF f
0.111
0.040
0.038
0.036
0.034
0.032
0.030
0.000
z
x
y
(c)
VVF f
0.123
0.040
0.038
0.036
0.034
0.032
0.030
0.000
z
x
y
(d)

Figure 10

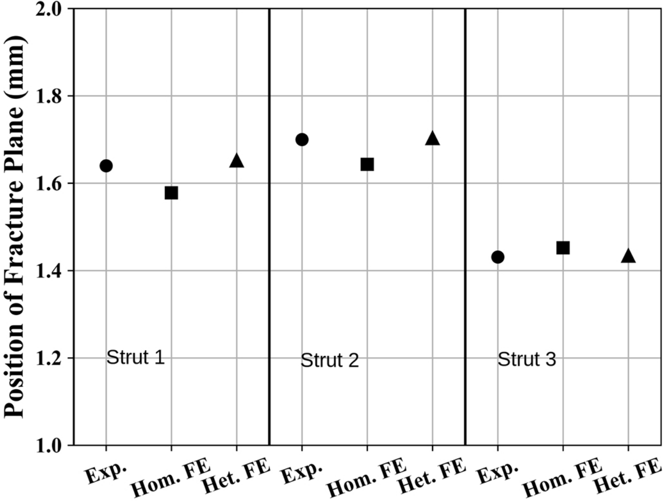
Position of Fracture Plane (mm)
2.0
1.8
1.6
1.4
1.2
1.0
Strut 1
Strut 2
Strut 3
Exp.
Hom. FE
Het. FE
Exp.
Hom. FE
Het. FE
Exp.
Hom. FE
Het. FE

Figure 11